

# Microstructural effect on the corrosion behavior of n- and p-type bismuth tellurides fabricated by induction melting

Farah M. El-Makaty<sup>a,1</sup>, Muddasir Nawaz<sup>b,1</sup>, R.A. Shakoor<sup>a,b,\*\*</sup>, Abdelmagid Hammuda<sup>a</sup>, Khaled M. Youssef<sup>a,c,\*</sup>

<sup>a</sup> Mechanical and Industrial Engineering Department, Qatar University, Doha 2713, Qatar

<sup>b</sup> Center for Advanced Materials (CAM), Qatar University, Doha 2713, Qatar

<sup>c</sup> Materials Science and Technology Graduate Program, College of Arts and Sciences, Qatar University, Doha 2713, Qatar

## ARTICLE INFO

### Keywords:

Corrosion  
Induction melting  
Bismuth telluride  
Microstructure

## ABSTRACT

Numerous efforts have been made to understand and enhance the thermoelectric properties of bismuth telluride alloys. However, limited studies have been reported to investigate the corrosion behavior of these alloys and their suitability for industrial applications. This paper examines the corrosion behavior of three different bismuth telluride alloys prepared by induction melting: pristine Bi<sub>2</sub>Te<sub>3</sub>, n-type Bi<sub>2</sub>Te<sub>2.55</sub>Se<sub>0.45</sub>, and p-type Bi<sub>0.6</sub>Sb<sub>1.4</sub>Te<sub>3</sub>. The electrochemical response of the samples is tested in 3.5 wt% NaCl solution at room temperature. Potentiodynamic polarization curves (Tafel plots) revealed that the n-type sample formed a passive layer compared to the pristine and the p-type samples, which showed pitting corrosion. The different trends observed in the samples were related to their evolved microstructures, where fingerprint-like features in the pristine and the p-type samples showed high susceptibility to pitting corrosion. In contrast, a unique needle-like microstructure of the n-type samples acted as nucleation sites for passive layer formation causing higher corrosion resistance in this sample.

## 1. Introduction

Bismuth telluride (Bi<sub>2</sub>Te<sub>3</sub>) and its alloys are considered to be the most efficient thermoelectric (TE) materials for near-room temperature applications [1]. The unique properties of Bi<sub>2</sub>Te<sub>3</sub> alloys result from their layered structure, which causes low thermal conductivity, tunable mobility, and low band gap leading to high electrical conductivity. However, to be implemented in devices, Bi<sub>2</sub>Te<sub>3</sub> alloys must be doped to become either electrons-based charge carriers (n-type) or holes-based charge carriers (p-type). The most common doping elements are selenium (Se, Bi<sub>2</sub>(Te<sub>1-x</sub>Se<sub>x</sub>)<sub>3</sub>) for the n-type and antimony (Sb, (Bi<sub>x</sub>Sb<sub>1-x</sub>)<sub>2</sub>Te<sub>3</sub>) for the p-type [2].

Massive efforts have been made to understand and improve the TE properties of Bi<sub>2</sub>Te<sub>3</sub> alloys. However, some key application properties, such as corrosion behavior, have yet to receive appropriate consideration. Depending on the operating conditions and the surrounding environment, atmospheric water may condense on the surface of

thermoelectric materials while in service leading to corrosion that could affect the device's maintenance and lifetime. Hence, to evaluate the actual capability in technological and industrial applications, it is critical to assess the corrosion behavior of these alloys.

A limited number of research studies on the electrochemical and corrosion behaviors of Bi<sub>2</sub>Te<sub>3</sub> alloys have been reported in the literature [3–6]. For example, Rosalbino et al. [3] studied the corrosion behavior of PbTe, Bi<sub>2</sub>Te<sub>3</sub>, and Sb<sub>2</sub>Te<sub>3</sub> compounds in a naturally aerated 0.1 M NaCl solution prepared by casting technique. Their results indicated higher resistance for the PbTe intermetallic compound than that of the Bi<sub>2</sub>Te<sub>3</sub> and Sb<sub>2</sub>Te<sub>3</sub> compounds due to the formation of a stable layer of corrosion products. Another study by Keshavarz et al. [4] focused on the effect of nano compositing of Bi<sub>1.9</sub>Sb<sub>0.1</sub>Te<sub>2.85</sub>Se<sub>0.15</sub> with MoS<sub>2</sub> nanoparticles produced by mechanical milling and hot extrusion on the corrosion properties. The outcomes revealed improved passivity of the nanocomposite compared with the coarse-grained single-phase alloy. However, to the best of our knowledge, no study has investigated the

\* Corresponding author at: Materials Science and Technology Graduate Program, College of Arts and Sciences, Qatar University, Doha 2713, Qatar.

\*\* Corresponding author: Center for Advanced Materials (CAM), Qatar University, Qatar.

E-mail addresses: [shakoor@qu.edu.qa](mailto:shakoor@qu.edu.qa) (R.A. Shakoor), [kyoussef@qu.edu.qa](mailto:kyoussef@qu.edu.qa) (K.M. Youssef).

<sup>1</sup> contributed equally.

influence of microstructure on the corrosion behavior of  $\text{Bi}_2\text{Te}_3$ .

In the present work, the corrosion behavior for undoped  $\text{Bi}_2\text{Te}_3$  and two optimized doped alloys,  $\text{Bi}_2\text{Te}_{2.55}\text{Se}_{0.45}$  (n-type) and  $\text{Bi}_{0.4}\text{Sb}_{1.6}\text{Te}_3$  (p-type), fabricated by induction melting is explored. The chosen compositions for the n- and p-type alloys are based on recent reported compositions which are expected to have optimum thermoelectric performance [2,7,8]. In addition, the study evaluates the electrochemical responses in 3.5 wt% NaCl solution at room temperature through potentiodynamic polarization and electrochemical impedance spectroscopy (EIS).

## 2. Methodology

### 2.1. Materials and synthesis of $\text{Bi}_2\text{Te}_3$ , $\text{Bi}_{0.4}\text{Sb}_{1.6}\text{Te}_3$ and of $\text{Bi}_2\text{Te}_{2.55}\text{Se}_{0.45}$ samples

Pure elemental shots of bismuth (purity 5 N), tellurium (2–5 mm, purity 5 N), antimony (1–3 mm, purity 6 N,) and selenium (purity 5 N) from ESPI Metals were used to prepare three different alloys:  $\text{Bi}_2\text{Te}_3$ ,  $\text{Bi}_{0.4}\text{Sb}_{1.6}\text{Te}_3$  (p-type) and  $\text{Bi}_2\text{Te}_{2.55}\text{Se}_{0.45}$  (n-type). The weighted elements were added into an 18 mm tungsten carbide die and sealed in a silica tube under a high-purity argon atmosphere. Before melting the alloys, a pure titanium getter was heated to ensure an oxygen-free atmosphere in the sealed quartz tube by using an induction furnace (Edmund Buhler GmbH, Germany). The samples were then heated, one at a time, as the current power was increased gradually to 30% and maintained for a few seconds until the sample was entirely melted. The melting process was repeated two times to ensure complete mixing.

To produce flat and dense discs, the samples were hot pressed (HP) under an argon atmosphere using an 18 mm tungsten carbide die. A temperature of 350 °C and a pressure of 0.8 GPa were applied for 10 min. Then the sample was left to cool to room temperature. Finally, the homogenization process for the three discs was done in a tube furnace (GSL-1500×-RTP50) under a mixed gas (2% hydrogen, 98% argon) atmosphere. The homogenization process was carried out at 300 °C for 6 h under a mixed gas (2% hydrogen, 98% argon), then air cooled.

### 2.2. Characterization

The microstructure of the prepared discs was analyzed by etching the samples with 10 mL  $\text{HNO}_3$  and 10 mL HCl for 10 s and then rinsing them with acetic acid and water. An optical microscope (BX53M OLYMPUS, Japan) was used to at different magnifications of 50×, 100×, and 200× to reveal the microstructures of the samples at different conditions (produced discs after homogenization, after etching, and after electrochemical tests). Scanning electron microscopy (SEM) (Nano-SEM Nova 450, FEI-USA) equipped with energy dispersive X-ray spectroscopy (EDS) was used to visualize the elemental distribution and obtain the elemental composition. In addition, X-ray photoelectron spectroscopy (XPS) (AXIS Ultra DLD by Kratos, US) analysis was done to study the chemical state of atoms after corrosion.

#### 2.2.1. Electrochemical properties measurements

Before each electrochemical test, the surface of the samples was mechanically ground using 600, 800, and 1200 SiC abrasive papers and then polished with 0.05 μm alumina suspension until a mirror surface was achieved.

The electrochemical tests were performed using Gamry Instruments (Reference 3000, USA). A standard three-electrode cell was used with an exposed area of 0.765 cm<sup>2</sup> containing a reference silver/silver chloride electrode and a graphite rod as a counter electrode. The electrolyte used is a naturally aerated 3.5% NaCl solution. All experiments were performed at 25 °C. Open circuit potential measurements were done for 1000s on freshly polished samples. Potentiodynamic polarization curves were studied from −200 to +900 mV vs. Ag/AgCl reference electrode at a scan rate of 1 mV/s. The electrochemical impedance (EIS) test was

measured for a frequency range of 100 kHz up to 10 mHz with 10 points per decade and a width of 10 mV rms for the applied sinusoidal voltage signal.

## 3. Results and discussion

### 3.1. Pre-test analysis of the samples

The phase composition of the three different samples, undoped  $\text{Bi}_2\text{Te}_3$ , p-type  $\text{Bi}_{0.4}\text{Sb}_{1.6}\text{Te}_3$ , and n-type  $\text{Bi}_2\text{Te}_{2.55}\text{Se}_{0.45}$  was characterized by XRD, as shown in Fig. 1. All the peaks obtained were well fitted by rhombohedral single-phase polycrystalline alloys (space group R-3 m)  $\text{Bi}_2\text{Te}_3$ ,  $\text{Bi}_{0.5}\text{Sb}_{1.5}\text{Te}_3$ , and  $\text{Bi}_2\text{Te}_{2.55}\text{Se}_{0.45}$  with X'Pert HighScore Plus reference codes 01–072-2036, 00–050-0954, and 00–049-1713, respectively [9]. Extra peaks in the  $\text{Bi}_{0.5}\text{Sb}_{1.5}\text{Te}_3$  sample were observed and identified as  $\text{Sb}_2\text{Te}_3$  phase (reference code: 01–071-0393). In addition, the XRD results were quantified by calculating the texture coefficient  $T_{c(hkl)}$  based on five peaks (015), (1010), (110), (0015), and (205). The  $T_{c(hkl)}$  factor was calculated for each orientation using [10]:

$$T_{c(hkl)} = \frac{I_{(hkl)}/I_{0(hkl)}}{(1/N) \left[ \sum_N I_{(hkl)}/I_{0(hkl)} \right]} \quad (1)$$

where  $I_{(hkl)}$  is the measured intensity of the peak,  $I_{0(hkl)}$  is the relative intensity corresponding to the plane given in the reference data, and N is the number of reflections. Interestingly, the p-type sample showed a high  $T_{c(0015)}$  factor of 3.78, implying a preferred orientation on the (0015) plane. On another note, broader peaks are observed for the n-type  $\text{Bi}_2\text{Te}_{2.55}\text{Se}_{0.45}$  pattern compared to that of the undoped  $\text{Bi}_2\text{Te}_3$  and p-type  $\text{Bi}_{0.4}\text{Sb}_{1.6}\text{Te}_3$  samples. This can be attributed to the higher amount of lattice strain developed in this specimen, mainly related to its intrinsic defects [11].

In order to study the samples' morphology and analyze the elemental distribution of the prepared discs, SEM was performed, and the corresponding images are shown in Fig. 2. Homogenous distribution of the

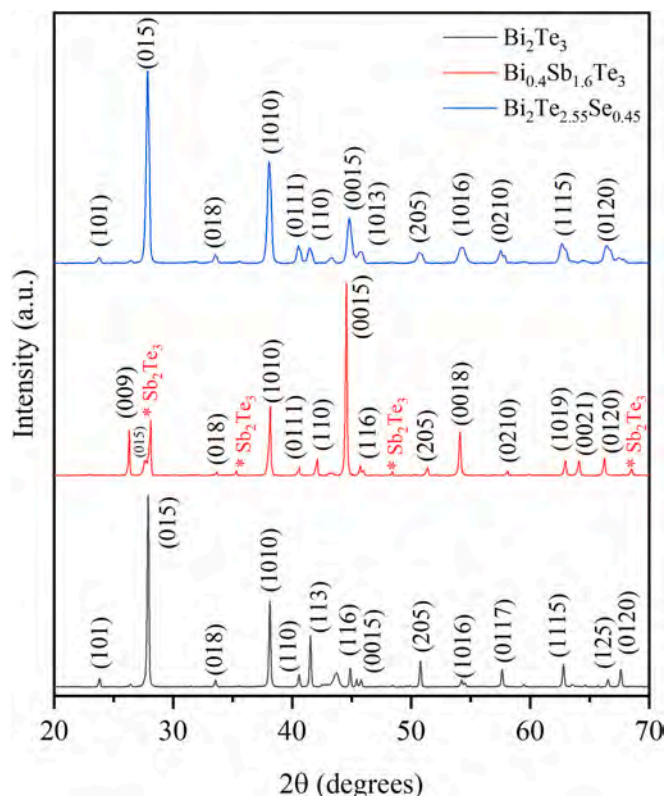


Fig. 1. XRD patterns for  $\text{Bi}_2\text{Te}_3$ ,  $\text{Bi}_{0.4}\text{Sb}_{1.6}\text{Te}_3$ , and  $\text{Bi}_2\text{Te}_{2.55}\text{Se}_{0.45}$  samples.

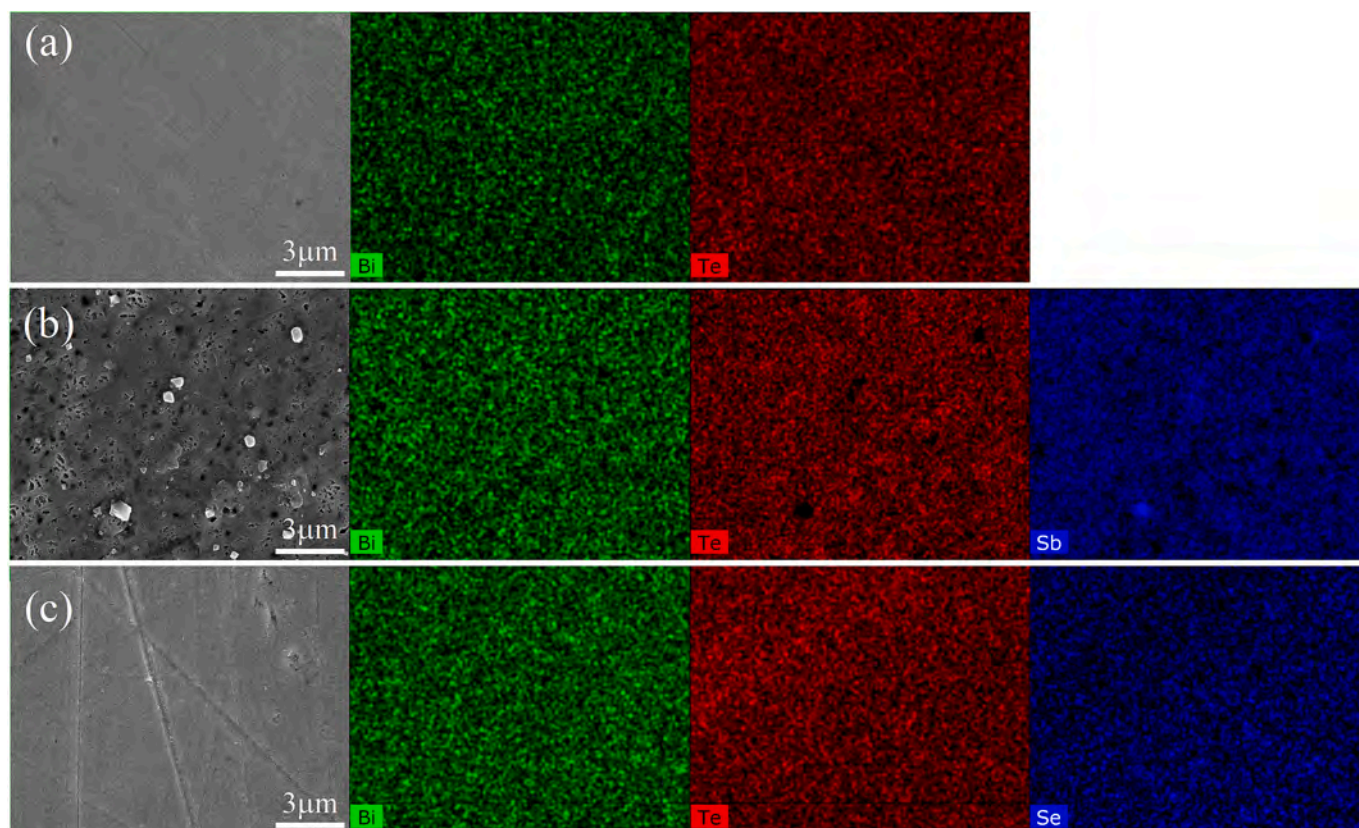


Fig. 2. SEM images and the corresponding elemental distribution for (a) undoped  $\text{Bi}_2\text{Te}_3$  (b)  $\text{Bi}_{0.4}\text{Sb}_{1.6}\text{Te}_3$  and (c)  $\text{Bi}_2\text{Te}_{2.55}\text{Se}_{0.45}$ .

elements was observed in the EDS mapping. However, the SEM images of p-type  $\text{Bi}_{0.4}\text{Sb}_{1.6}\text{Te}_3$  sample showed some porosity in the structure as well as small particles on the surface, which were identified as Sb rich precipitates from the elemental mapping and are consistent with the XRD. In fact, Siqi et al. [12] prepared several  $\text{Te}_{1-x}\text{Sb}_x$  alloys with various x amounts by a combination of ball-milling/hot-pressing techniques and noticed similar embedded Sb rich precipitates within the  $\text{Te}_{1-x}\text{Sb}_x$  matrixes. The authors reported that the precipitates have a Te: Sb ratio close to that of  $\text{Sb}_2\text{Te}_3$  and their size is within a few microns, matching well with our work. The results of their study proved the importance of these precipitates in improving the overall thermoelectric properties of the alloy. Yet the effect of such Sb rich precipitates on corrosion properties has not been explored, which adds another dimension to our current study. On another note, compositional data of the investigated alloys were also obtained by EDX are reported in Table 1, presenting a good agreement between nominal and experimental composition of the matrixes.

Moreover, the microstructure was revealed through etching, and the corresponding optical micrographs are shown in Fig. 3. The undoped  $\text{Bi}_2\text{Te}_3$  and the p-type alloys showed similar randomly oriented and elongated grains having fingerprint-like structures within the grains. On the other hand, the microstructure for the Se-doped n-type sample, interestingly, showed a randomly aligned needle-like structure. The dimensions of the needles are about 10–60  $\mu\text{m}$  in width and 300–900  $\mu\text{m}$

in length. The observed microstructure could have a significant impact on the corrosion behavior of the samples. Septimio et al. [13] prepared BiZn alloys with different Zn wt% via melting and water-cooled solidification. The authors reported distinct microstructural morphologies for different Zn contents, e.g., trigonal dendrite of 1.5 wt% Zn, eutectic mixture for 2.7 wt% Zn and hypereutectic alloy with needle-like structure for 5 wt% Zn. The main reason for the distinct microstructures was reported to be Zn amount and its distribution.

### 3.2. Electrochemical characterization for corrosion behavior

#### 3.2.1. Potentiostatic analysis

The corrosion resistance properties of the bismuth telluride alloys were investigated by the Potentiostatic EIS analysis in stagnant naturally aerated 3.5 wt% NaCl. Fig. 4 depicts the obtained raw and fitted impedance spectra. The plots showed that the samples had a capacitive response in a medium frequency range and a resistive response at higher frequencies. The phase angle shift of  $-55^\circ$  shows the semi-capacitive response due to the heterogeneity of the electrode surface [14]. The obtained results agree with the reported data by Rosalbino et al. [3]. Moreover, the low-frequency impedance value ( $|Z|_{0.01\text{Hz}}$ ) for the n-type sample is slightly higher, 17.7  $\text{k}\Omega$ , compared to 10.0 and 8.1  $\text{k}\Omega$  for p-type and pristine samples, respectively, suggesting higher corrosion resistance in the aggressive environment. Besides, the phase angle for p-type samples decreased at intermediate frequencies (0.1 to 100 Hz) indicating the shift from capacitive to resistive behavior [15]. This finding is also consistent with  $|Z|_{0.01\text{Hz}}$  value, the p-type alloy loses its corrosion protective behavior as compared to the pristine and the n-type alloy. Meanwhile, the n-type alloy owns a different trend with improvements in impedance value and a slight increase in the capacitive behavior due to the formation of a protective film on its surface [16]. This behavior could be attributed to its unique needle-like microstructure which causes higher corrosion resistance.

Table 1  
EDS analysis results for the samples (compared to nominal calculations).

Sample	$\text{Bi}_2\text{Te}_3$	$\text{Bi}_{0.4}\text{Sb}_{1.6}\text{Te}_3$	$\text{Bi}_2\text{Te}_{2.55}\text{Se}_{0.45}$
Bi (at.%)	41 (40)	8 (8)	41 (40)
Te (at.%)	59 (60)	33 (32)	51 (51)
Sb (at.%)	–	59 (60)	–
Se (at.%)	–	–	8 (9)



Fig. 3. Microstructure of the etched samples for (a) undoped  $\text{Bi}_2\text{Te}_3$  (b)  $\text{Bi}_{0.4}\text{Sb}_{1.6}\text{Te}_3$  and (c)  $\text{Bi}_2\text{Te}_{2.55}\text{Se}_{0.45}$ .

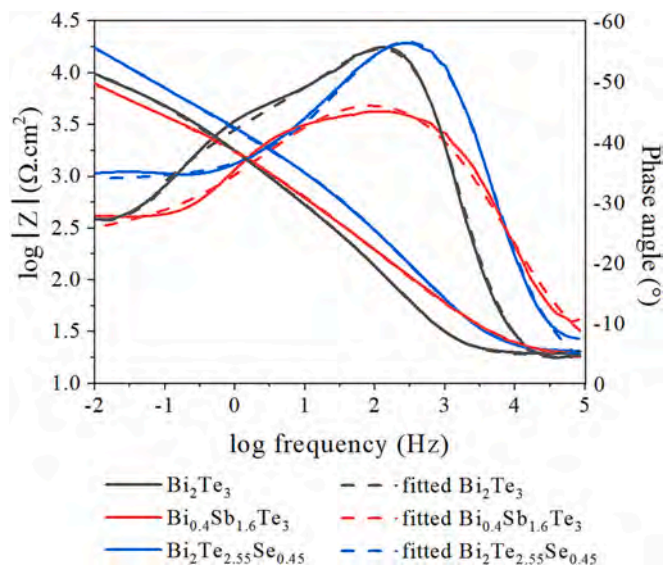


Fig. 4. Bode diagram for the investigated bismuth telluride alloys in naturally aerated stagnant 3.5 wt% NaCl solution.

### 3.2.2. Equivalent electric circuit fitting

Two-time constants with a Warburg equivalent circuit were used for the fitting and assessments of EIS parameters from the EIS analysis spectra. It can be observed from Fig. 4 that at intermediate frequency ranges, there exist a linear relationship between  $\log |Z|$  and  $\log$  frequency with slopes close to 1 as well as a phase angle with a peak lower than  $90^\circ$ , suggesting that the formed passive films do not act as ideal capacitors [17]. Hence, constant phase elements (CPE) were introduced for fitting the spectra, whose impedance is defined as in eq. 2.

$$Z_{CPE} = [Q(j\omega)^n]^{-1} \tag{2}$$

where  $\omega$  is the angular frequency (rad/s),  $Q$  is a constant,  $j$  is an imaginary number, and  $n$  is the exponent for the CPE. The exponent  $n$  has values between  $-1$  and  $1$ ; where the values  $-1$ ,  $0$ ,  $0.5$ , and  $1$  correspond to an inductor, resistor, diffusion, and capacitor behaviors, respectively. Based on the reasons mentioned, the equivalent electrical circuit (EEC) presented in Fig. 5 was proposed to fit the data. The circuit consists of one resistor representing the solution resistance ( $R_{sol}$ ), and two other resistors ( $R_1$  and  $R_2$ ) accompanied by two CPEs ( $CPE_1$  and  $CPE_2$ ) connected in parallel.

As shown in Fig. 4, the fitting of the proposed model is very close to the raw data with a chi-squared value of  $10^{-6}$ , which shows better fitting, implying that the EEC employed is representative of the corrosion mechanisms occurring. Even though the three samples were well-fitted using the same model, the physical meaning of the EEC is different in the samples. For pristine  $\text{Bi}_2\text{Te}_3$  and n-type samples,  $R_1$  and  $CPE_1$  correspond to the semiconductor corrosion ( $R_{scc}$ ,  $CPE_{scc}$ ), while  $R_2$  and  $CPE_2$  represent the passive films formed by anti-corrosion products ( $R_{pf}$ ,  $CPE_{pf}$ ), such as oxides or oxychlorides layers and Warburg ( $W$ ) corresponds to the diffusion of ions (Fig. 6a). Since the p-type sample has no passive layer formation, the physical meaning of the ECC in this sample can be related to the semiconductor corrosion ( $R_{scc}$ ,  $CPE_{scc}$ ) and resistance coming from the oxide's layers formed during corrosion ( $R_{nlm}$ ,  $CPE_{nlm}$ ) (Fig. 6b). The fitting parameters values obtained after the fitting with the proposed EEC are presented in Table 2, which shows that the pristine and n-type were effective in blocking the active species from accessing the electrode surface, limiting ion diffusion to the surface, and decreasing the corrosion rate. By comparing the  $R_{scc}$  value for the three samples, it can be concluded that doping of  $\text{Bi}_2\text{Te}_3$  enhances the resistance value of n-type to  $10.41 \text{ k}\Omega/\text{cm}^2$ , while it slightly decreased to  $3.92 \text{ k}\Omega/\text{cm}^2$  for the p-type. This can be explained by the increased charge carrier concentration, where more electrons/holes are free for

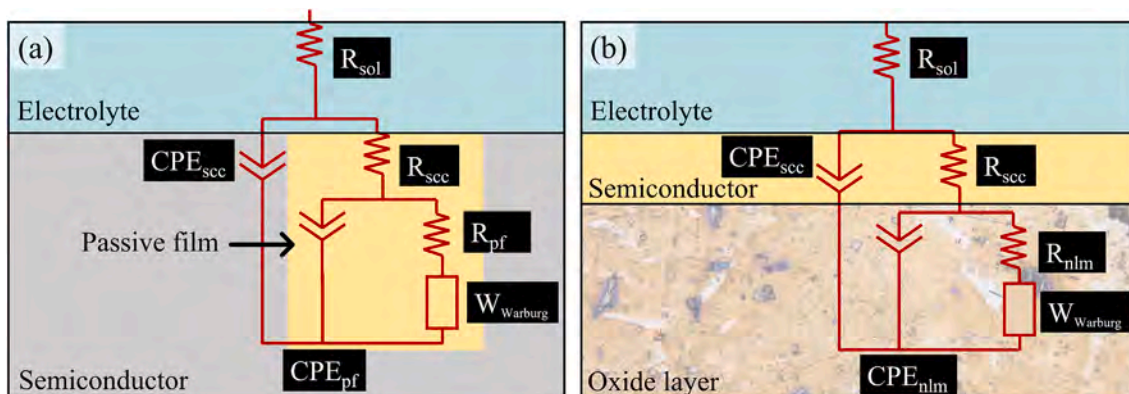


Fig. 5. Equivalent electrical circuit employed to model EIS data.

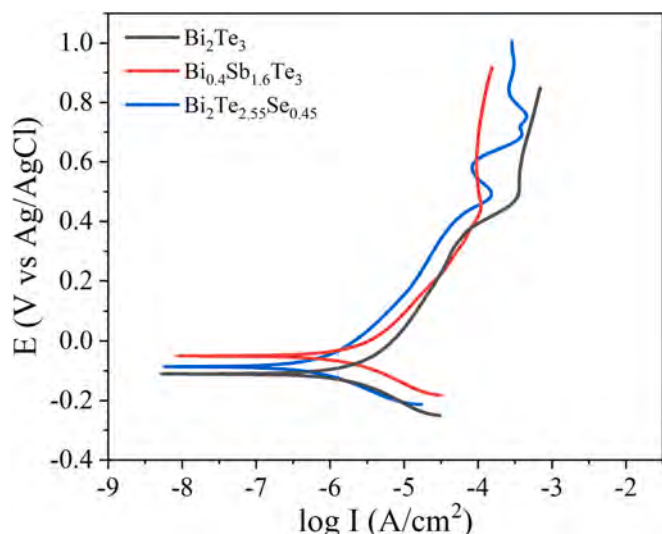


Fig. 6. Potentiodynamic polarization curves measured for the investigated bismuth telluride samples in naturally aerated stagnant 3.5 wt% NaCl solution.

the diffusion process [18].

The  $CPE_{sc}$  value for  $Bi_2Te_3$  and doped (p-type and n-type) remains the same and a significant difference was observed. Moreover, the value of  $R_{pf}$  for the pristine  $Bi_2Te_3$  and p-type samples almost remains the same, while it increased to  $491.1 \Omega/cm^2$  as compared to pristine  $292.9 \Omega/cm^2$ . The increase in resistance is due to the formation of the passive film for the n-type. Moreover, the  $CPE_{pf}$  value for the n-type sample was observed to be  $1.40 \times 10^{-5}$  as compared to  $7.18 \times 10^{-5}$  for the p-type sample. However, interestingly the value of  $n_2$  component increased to 0.89 which could be due to the presence of a protective layer formed on the surface of  $Bi_2Te_{2.55}Se_{0.45}$ . This increase in  $n_2$  value is also consistent with capacitive behavior observed in phase angle. Higher resistance and lower capacitance values indicate better corrosion protective property of the sample. The lower diffusion value  $3.18 \times 10^{-4}$  for the n-type sample as compared to other samples also suggest less corrosion activity on the sample surface due to its protective film formation [19].

### 3.2.3. Potentiodynamic analysis

A Potentiodynamic polarization test was carried out to investigate the corrosion activity of bismuth telluride alloys in naturally aerated stagnant 3.5 wt% NaCl solution (Fig. 6). The corresponding electrochemical parameters i.e., electrode potential ( $E_{corr}$ ), current density ( $I_{corr}$ ), corrosion rate and polarization resistance ( $R_p$ ), were calculated from the polarization curve using OriginPro software and presented in Table 3. The slope of linear anodic and cathodic curves was used to find  $\beta_a$  and  $\beta_c$ , respectively. The intersection resulting from extrapolating the linear slopes was used to find  $I_{corr}$  and  $E_{corr}$  values. The corrosion rate [20] was calculated from eq. 3.

$$Corrosion\ rate\ (mpy) = 0.13 I_{corr} \times \frac{EW}{d} \tag{3}$$

where  $EW$  and  $d$  are the equivalent weight and density of the samples, respectively. Lastly, Eq. (4) was used for polarization resistance calculations [21].

Table 2

Parameters obtained for the equivalent electric circuit by fitting the EIS data.

Sample	$R_{sc}$ ( $k\Omega/cm^2$ )	$CPE_{sc}$ ( $F\ S^{-1}\ cm^2$ )	$n_1$	$R_{pf}$ ( $\Omega/cm^2$ )	$CPE_{pf}$ ( $F\ S^{-1}\ cm^2$ )	$R_{nlm}$ ( $k\Omega/cm^2$ )	$CPE_{nlm}$ ( $F\ S^{-1}\ cm^2$ )	$n_2$	$W$
$Bi_2Te_3$	6.24	$2.17 \times 10^{-4}$	0.50	292.9	$2.52 \times 10^{-5}$	-	-	0.81	$8.21 \times 10^{-4}$
$Bi_{0.4}Sb_{1.6}Te_3$	3.92	$1.39 \times 10^{-4}$	0.45	297.2	$7.18 \times 10^{-5}$	-	-	0.63	$8.07 \times 10^{-4}$
$Bi_2Te_{2.55}Se_{0.45}$	10.41	$2.34 \times 10^{-4}$	0.38	-	-	491.9	$1.40 \times 10^{-5}$	0.89	$3.18 \times 10^{-4}$

$$R_p = \frac{\beta_a \beta_c}{2.3 I_{corr} (\beta_a + \beta_c)} \tag{4}$$

Fig. 6 shows that the shape of polarization curves is quite similar for undoped  $Bi_2Te_3$  and p-type samples exhibiting a similar trend. For these two samples, p-type alloy showed slightly better corrosion potential ( $E_{corr}$ ) as compared to other samples. However, the n-type sample exhibited the lowest corrosion current density and corrosion rate values compared to the undoped  $Bi_2Te_3$  and the p-type samples. The low current density leads to a weak electron transfer capability which reflects the better corrosion property of the sample. Furthermore, an effective development of a protective film on the sample surface has significantly reduced the electron transfer, which eventually decreased the corrosion rate and led to significant inhibition of corrosion activities. Keshavarz et al. [4] studied the corrosion behavior in 3.5 wt% NaCl of n-type  $Bi_{1.9}Sb_{0.1}Te_{2.85}Se_{0.15}$  prepared by mechanical alloying and hot extrusion. The authors reported a corrosion current density of  $1.27 \mu A/cm^2$  and a corrosion potential of  $-141\ mV/(Ag/AgCl)$ . It is worth noting that the n-type sample prepared in our study has much lower  $I_{corr}$  values ( $0.56 \mu A/cm^2$ ) which could possibly be resulted due to (i) the different preparation technique and the resulted unique needle-like microstructure, and (ii) doping with Se only and not including Sb in the alloy, as seen in Table 3, the sample doped with Sb had higher  $I_{corr}$ . The measured polarization resistance ( $R_p$ ) from the above eq. 4 shows that undoped  $Bi_2Te_3$  and p-type  $Bi_{0.4}Sb_{1.6}Te_3$  are close to each other, while n-type  $Bi_2Te_{2.55}Se_{0.45}$  shows more than 2-time higher value, which agreeing well with the results of  $I_{corr}$  values and emphasizing the role of microstructure on the corrosion behavior of the samples.

### 3.3. Post-test analysis of the samples

Images of the discs before and after electrochemical testing and their corresponding optical micrographs are presented in Fig. 7. The pristine  $Bi_2Te_3$  alloy encountered an increase in surface porosity, which could be attributed to pitting corrosion. For the p-type sample, a brownish layer was formed on some of the exposed area, accompanied by an increase in the size of pores presented beforehand. These observations suggest that the finger-like microstructure seen in these samples (Fig. 3a-b) is more susceptible to the corrosion pitting phenomenon. Meanwhile, the n-type sample showed a protective film on its surface in a dark black layer, supporting the discussed results of electrochemical testing. No corrosion activity and corrosion pits were observed for the n-type sample. Fig. 8 shows the microscopic images of the n-type sample for in-depth study, which reveals the surface under the black layer, a needle-like microstructure of the sample was observed, indicating that the microstructure acted as nucleation sites for passive layer formation.

Table 3

Electrochemical parameters obtained from the Potentiodynamic polarization curves of the investigated bismuth telluride samples tested in naturally aerated 3.5 wt% NaCl solution.

Sample	$E_{corr}$ (mV/(ag/AgCl))	$i_{corr}$ ( $\mu A/cm^2$ )	Corrosion rate (mpy)	$R_p$ ( $\Omega$ )
$Bi_2Te_3$	-112	1.7	0.832	18.8
$Bi_{0.4}Sb_{1.6}Te_3$	-50.2	1.4	0.642	19.1
$Bi_2Te_{2.55}Se_{0.45}$	-86.7	0.56	0.262	47.4

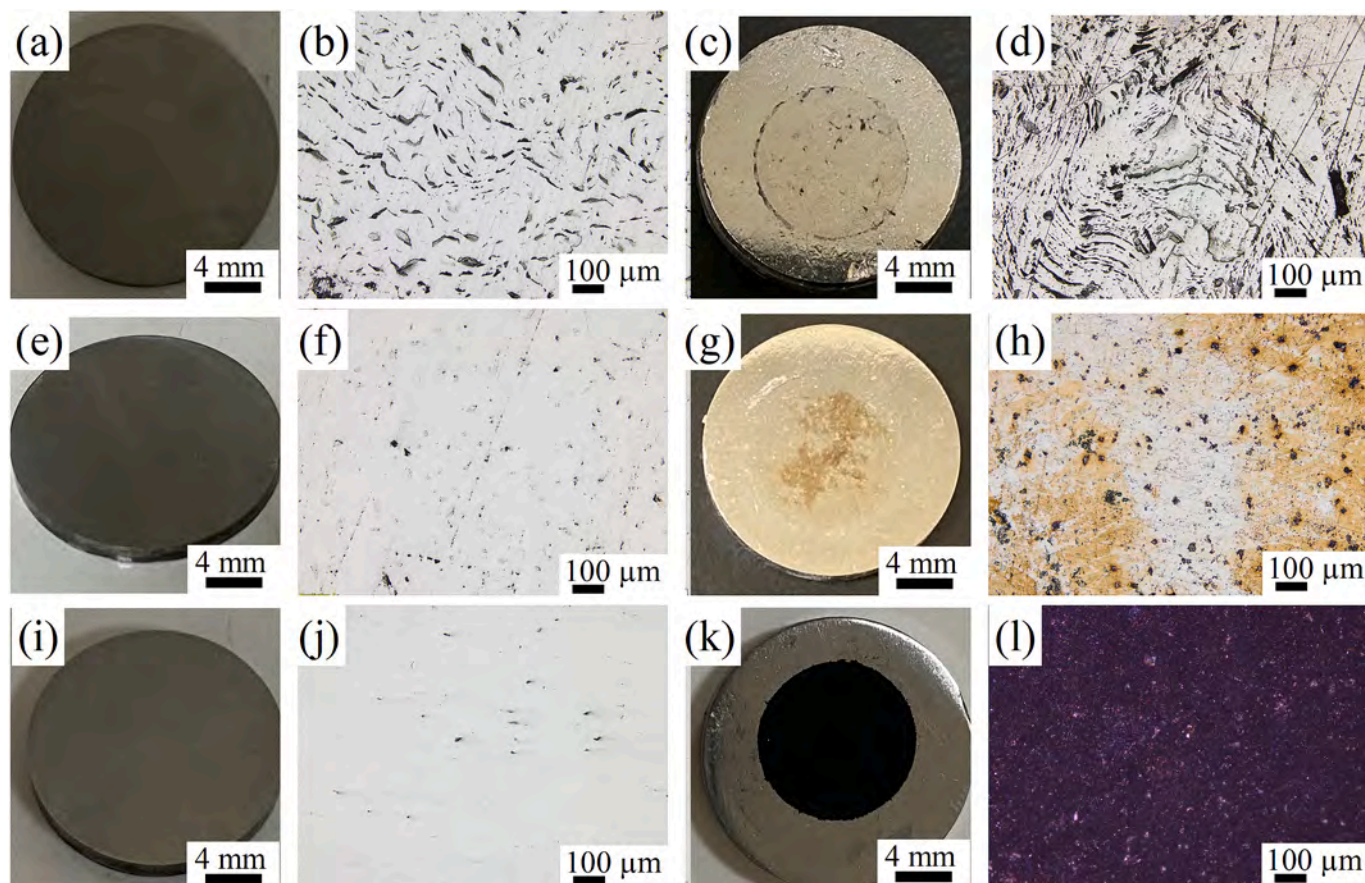


Fig. 7. Discs before (left) and after (right) corrosion and their corresponding optical images for (a-d) undoped  $\text{Bi}_2\text{Te}_3$  (e-h)  $\text{Bi}_{0.4}\text{Sb}_{1.6}\text{Te}_3$  and (i-l)  $\text{Bi}_2\text{Te}_{2.55}\text{Se}_{0.45}$ .

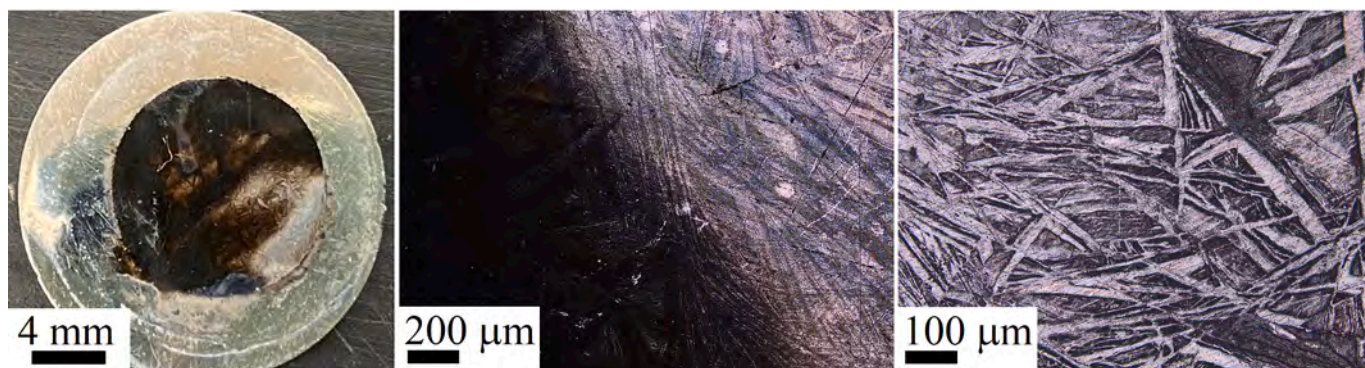


Fig. 8. N-type  $\text{Bi}_2\text{Te}_{2.55}\text{Se}_{0.45}$  disc after corrosion and its optical micrographs.

Furthermore, the XPS analysis was performed to study the nature of the black and yellowish layers formed on the n- and p-type discs after electrochemical testing. These results are illustrated in Fig. 9. High-resolution spectra of Bi 4f, Te 3d, Se 3d and Sb 3d were obtained using C 1 s as a reference at 285 eV. Fig. 9a-c reveals that the dark black layer formed on the surface of the n-type  $\text{Bi}_2\text{Te}_{2.55}\text{Se}_{0.45}$  sample consists of  $\text{Bi}_2\text{O}_3$  [22,23] and  $\text{TeO}_2$  [24] oxides as well as a Te 3d bond. The Te  $3d_{3/2}$  and  $3d_{5/2}$  peaks at 582.6 and 573 eV, respectively, correspond to tellurium impurity. It is noteworthy that Se did not contribute to forming any corrosion products. On the other hand, the yellowish corrosion layer on the p-type  $\text{Bi}_{0.4}\text{Sb}_{1.6}\text{Te}_3$  sample consists of  $\text{Bi}_2\text{O}_3$ ,  $\text{Sb}_2\text{O}_3$  [25], and  $\text{TeO}_2$  oxides (Fig. 9d-f).

#### 4. Conclusion

In summary, the corrosion behavior of three different bismuth telluride alloys ( $\text{Bi}_2\text{Te}_3$ ,  $\text{Bi}_2\text{Te}_{2.55}\text{Se}_{0.45}$ , and  $\text{Bi}_{0.6}\text{Sb}_{1.4}\text{Te}_3$ ) in 3.5 wt% NaCl solution was investigated. The EIS results revealed that passive film formation led to the capacitive behavior for the n-type sample. Potentiodynamic polarization curves show the lower corrosion current density and corrosion rate for the n-type sample due to the development of a protective film on its surface. The polarization resistance for the n-type sample is twice as compared to the p-type sample due to needle-like microstructure, which caused higher corrosion resistance with nucleation sites for passive layer formation. The results also showed that the finger-like microstructure of undoped  $\text{Bi}_2\text{Te}_3$  and p-type  $\text{Bi}_{0.6}\text{Sb}_{1.4}\text{Te}_3$  samples led to pitting corrosion. The discussed results prove the

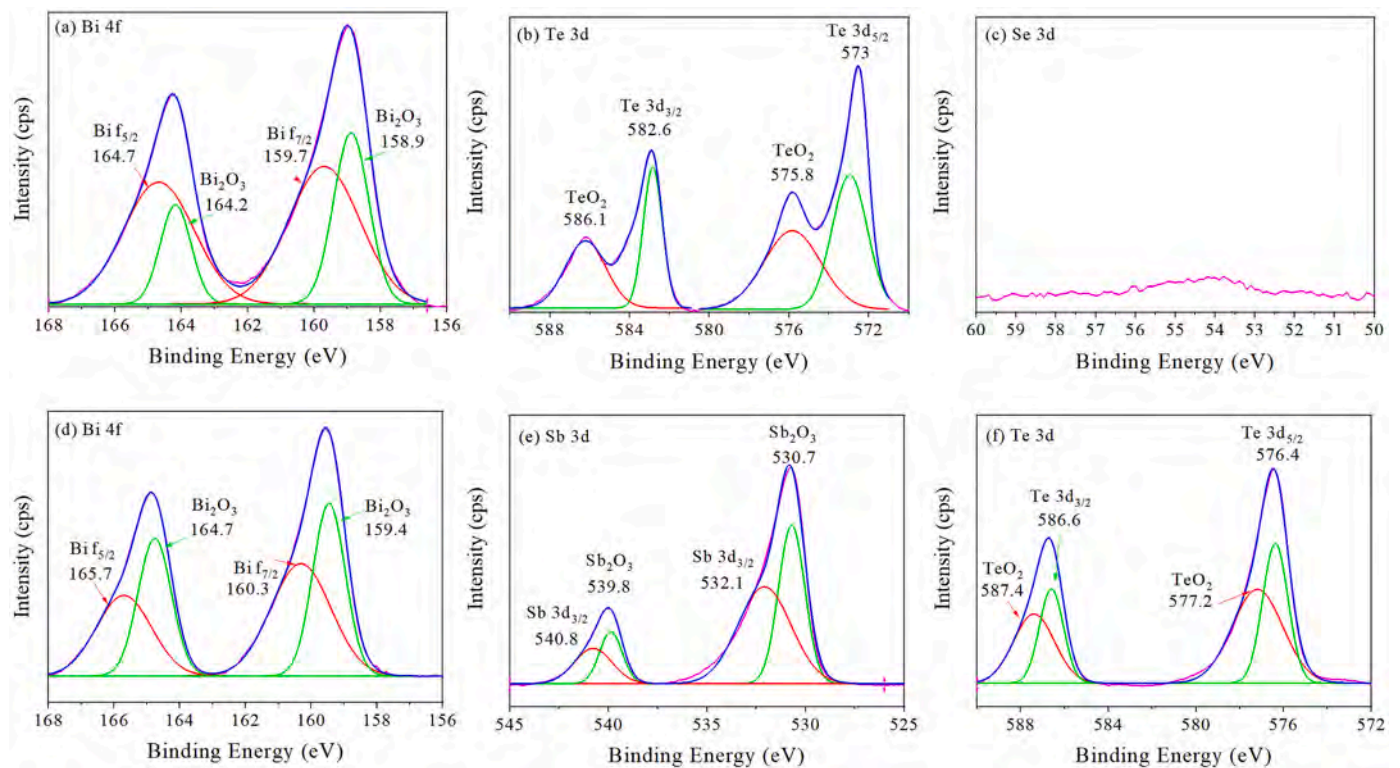


Fig. 9. XPS spectra for n-type  $\text{Bi}_2\text{Te}_{2.55}\text{Se}_{0.45}$  disc (a) Bi 4f, (b) Te 3d, and (c) Se 3d, and p-type  $\text{Bi}_{0.4}\text{Sb}_{1.6}\text{Te}_3$  disc (d) Bi 4f, (e) Sb 3d, and (f) Te 3d after electrochemical testing.

importance of microstructure in determining the type of corrosion occurring in bismuth telluride alloys.

#### Declaration of Competing Interest

The authors declare that they have no known competing financial interests or personal relationships that could have appeared to influence the work reported in this paper.

#### Data availability

Data will be made available on request.

#### Acknowledgments

This work was supported by Grant no. NPRP10–0206–170366 and GSR8-L-1-0414-21013 from Qatar National Research Fund (a member of the Qatar Foundation). The statements made herein are solely the responsibility of the authors. The authors acknowledge the technical support from the Central Laboratory Unit (CLU), the Center of Advanced Materials (CAM), and the Chemistry Department at Qatar University. Open Access funding is provided by the Qatar National Library.

#### References

- [1] F.M. El-Makaty, K. Andre Mkhoyan, K.M. Youssef, The effects of structural integrity of graphene on the thermoelectric properties of the n-type bismuth-telluride alloy, *J. Alloys Compd.* 876 (2021), 160198.
- [2] F.M. El-Makaty, H.K. Ahmed, K.M. Youssef, Review: the effect of different nanofiller materials on the thermoelectric behavior of bismuth telluride, *Mater. Des.* 209 (2021), 109974.
- [3] F. Rosalbino, R. Carlini, G. Zanicchi, G. Scavino, Microstructural characterization and corrosion behavior of lead, bismuth and antimony tellurides prepared by melting, *J. Alloys Compd.* 567 (2013) 26–32.
- [4] M.K. Keshavarz, A. Fattah-alhosseini, Electrochemical response of n-type bismuth telluride based thermoelectric materials in NaCl solutions: a comparison between a single-phase alloy and a nanocomposite containing  $\text{MoS}_2$  nano-particles, *Arab. J. Chem.* 13 (1) (2020) 1858–1865.
- [5] H. Kohri, T. Yagasaki, Corrosion Behavior of  $\text{Bi}_2\text{Te}_3$ -Based Thermoelectric Materials Fabricated by Melting Method 46(5), 2017, pp. 2587–2592.
- [6] H.-P. Feng, B. Yu, S. Chen, K. Collins, C. He, Z.F. Ren, et al., Studies on Surface Preparation and Smoothness of Nanostructured  $\text{Bi}_2\text{Te}_3$ -Based Alloys by Electrochemical and Mechanical Methods 56(8), 2011, pp. 3079–3084.
- [7] A.-Y. Eum, I.-h. Kim, S.-M. Choi, S. Lee, W.S. Seo, J.-S. Park, et al., Thermoelectric and transport properties of mechanically-alloyed  $\text{Bi}_2\text{Te}_3$ -ySe solid solutions, *J. Korean Phys. Soc.* 67 (2015) 1809–1813.
- [8] A.S. Lemine, F.M. El-Makaty, H.A. Al-Ghanim, K.M. Youssef, Experimental and modeling analysis of p-type  $\text{Bi}_{0.4}\text{Sb}_{1.6}\text{Te}_3$  and graphene nanocomposites, *J. Mater. Res. Technol.* 16 (2022) 1702–1712.
- [9] T. DegenMS, E. Bron, U. König, G. Nénert, The HighScore suite, *Powder Diffraction* 29 (S 2) (2014). S 13-S 8.
- [10] J. Sakalinen, J. Yvien, B. Abakeviien, J. Dudonis, Investigation of Structural and Optical Properties of GDC Thin Films Deposited by Reactive Magnetron Sputtering 120(1), 2011, pp. 63–65.
- [11] B. Zhu, Y. Yu, X.-y. Wang, F.-q. Zu, Z.-y. Huang, Enhanced thermoelectric properties of n-type  $\text{BiTeSe}$  semiconductor by manipulating its parent liquid state, *J. Mater. Sci.* 52 (14) (2017) 8526–8537.
- [12] S. Lin, W. Li, X. Zhang, J. Li, Z. Chen, Y. Pei, Sb induces both doping and precipitation for improving the thermoelectric performance of elemental Te, *Inorg. Chem. Front.* 4 (6) (2017) 1066–1072.
- [13] R.S. Septimio, M.A. Arenas, A. Conde, A. Garcia, N. Cheung, J.D. Damborenea, Correlation between Microstructure and Corrosion Behaviour of Bi-Zn Solder Alloys 54(4), 2019, pp. 362–368.
- [14] P. Tamási, G. Kósa, B. Szabó, R. Berényi, B. Medgyes, Effect of bismuth and silver on the corrosion behavior of lead-free solders in 3.5 wt%, NaCl Solut. 60 (4) (2016) 232–236.
- [15] M.K. Keshavarz, A. Fattah-Alhosseini, Effect of Immersion Time on Corrosion Behavior of Single-Phase Alloy and Nanocomposite Bismuth Telluride-Based Thermoelectrics in NaCl Solution 27(7), 2018, pp. 3386–3393.
- [16] N.W.B. Subri, M. Sarraf, B. Nasiri-Tabrizi, B. Ali, M.F. Mohd Sabri, W.J. Basirun, et al., Corrosion Insight of Iron and Bismuth Added Sn1Ag0.5Cu Lead-Free Solder Alloy 55(1), 2020, pp. 35–47.
- [17] S. Kumaraguru, E. Sundaravadeivel, Direct Electro-Synthesis of Rationally Designed, Sturdy NiPBi<sub>2</sub>O<sub>3</sub> Nanocomposite Coatings: Tailoring the Texture, Microhardness, and Corrosion Prevention Characteristics 48(19), 2022, pp. 28864–28873.
- [18] H.J. Goldsmid, Bismuth telluride and its alloys as materials for thermoelectric generation, *Materials (Basel)* 7 (4) (2014) 2577–2592.
- [19] H.A. Jaffery, M.F.M. Sabri, S.M. Said, S.W. Hasan, I.H. Sajid, N.I.M. Nordin, et al., Electrochemical Corrosion Behavior of Sn-0.7Cu Solder Alloy with the Addition of Bismuth and Iron, 2019, p. 810.

- [20] J. Majhi, S. Ganguly, A. Basu, A.K. Mondal, Improved Corrosion Response of Squeeze-Cast AZ91 Magnesium Alloy with Calcium and Bismuth Additions 873, 2021.
- [21] R. Spotorno, G. Ghiara, G. Latronico, R. Carlini, P. Mele, C. Artini, Corrosion of the Filled Skutterudite  $\text{Sm}_{0.1}(\text{Fe}_{0.45}\text{Ni}_{0.55})_4\text{Sb}_{12}$  by NaCl Solutions: An Electrochemical Study 49(5), 2020, pp. 2872–2880.
- [22] M. Ahmad, K. Agarwal, B.R. Mehta, An anomalously high Seebeck coefficient and power factor in ultrathin  $\text{Bi}_2\text{Te}_3$  film: spin–orbit interaction, *J. Appl. Phys.* 128 (3) (2020), 035108.
- [23] Y. Shi, L. Luo, Y. Zhang, Y. Chen, S. Wang, L. Li, et al., Synthesis and characterization of porous platelet-shaped  $\alpha\text{-Bi}_2\text{O}_3$  with enhanced photocatalytic activity for 17 $\alpha$ -ethynylestradiol, *J. Mater. Sci.* 53 (2) (2018) 1049–1064.
- [24] F. Lu, J. Wang, X. Sun, Z. Chang, 3D hierarchical carbon nanofibers/ $\text{TiO}_2$ @ $\text{MoS}_2$  core-shell heterostructures by electrospinning, hydrothermal and in-situ growth for flexible electrode materials, *Mater. Des.* 189 (2020), 108503.
- [25] L. Bodenes, A. Darwiche, L. Monconduit, H. Martínez, The solid electrolyte interphase a key parameter of the high performance of Sb in sodium-ion batteries: comparative X-ray photoelectron spectroscopy study of Sb/Na-ion and Sb/Li-ion batteries, *J. Power Sources* 273 (2015) 14–24.